Ahuir-Torres, JI, Meredith, A, Batako, AD, Kotadia, HR, Opoz, TT, Zhu, G, Khidasheli, N, Sharp, MC and Bakradze, N

Corrosion behaviour of hardened grey cast iron with continuous-wave infrared laser

Materials Today Communications 44 (2025) 111852

Contents lists available at ScienceDirect

Materials Today Communications

journal homepage: www.elsevier.com/locate/mtcomm

Corrosion behaviour of hardened grey cast iron with continuous-wave infrared laser

J.I. Ahuir-Torres [a,*], A. Meredith [b], A.D. Batako [a], H.R. Kotadia [b], T.T. Opoz [a], G. Zhu [c,e], Nugzar Khidasheli [d], M.C. Sharp [a], Nana Bakradze [d]

[a] General Engineering Research Institute, Faculty of Engineering and Technology, Liverpool John Moores University, Byrom Street, Liverpool L3 3AF, United Kingdom
[b] School of Engineering, Faculty of Engineering and Technology, Liverpool John Moores University, Byrom Street, Liverpool L3 3AF, United Kingdom
[c] School of Electrical Engineering, Chongqing University of Arts and Sciences, Chongqing 402159, China
[d] Depart. of Production Technologies of Mechanical Engineering, Georgian Technical University, 77 Kostava srt., Tbilisi 0175, Georgia
[e] Bishan Advanced Technology Research Institute of Chongqing University, No. 92 Bishan Donglin Avenue, Chongqing 402760, China

ARTICLE INFO

Keywords:
Laser Hardening
Grey cast iron
Corrosion resistance
Nobility
Hardness and corrosion mechanism evolution

ABSTRACT

Grey cast iron is employed under chemically and physically harsh conditions. Laser hardening is used to improve the material mechanical properties. The corrosion behaviour of laser hardened cast iron, however, needs to be studied in detail. This study is focused on the assessment of the hardness and corrosion resistance of the laser hardened grey cast iron. Laser hardening was conducted with a continuous-wave (CW) near infrared fibre laser. The corrosion evaluations were carried out with electrochemical analysis techniques. The laser hardened samples with 25 % scan overlap exhibited higher corrosion resistance and hardness than the as-received grey cast iron specimens.

1. Introduction

Grey cast iron presents a low cost, good castability and large range of mechanical properties [1,2]. This alloy is used under harsh conditions in several industries, such as automotive, maritime, mining and military [2–5]. Due to the aggressive work condition, grey cast iron is commonly hardened to improve its mechanical properties. This process can be carried out with various methods, such as annealing, laser, peening, coating, anodizing, electron beam, ion beam implant and ultrasonic [6,7].

Laser hardening is increasingly used to harden the metal owing to its good properties, such as reproducibility, accuracy, environmental friendly and ease of automation [5,8]. Various laser devices have been used to conduct the hardening process on grey cast iron, including carbon dioxide [5,9,10], Nd:YAG [5,9,11–13], solid state [14] and fibre [15–17]. These lasers usually work in continuous-wave [5,9,11–15,17] or pulsed [9,16,18] mode for the hardening processes. The continuous-wave infrared fibre lasers have become widely employed to harden cast iron components due to their ability to be integrated into robotic systems, permitting the hardening of complex structures [17,19–21]. The process modelling (e.g., finite elements) has facilitated increased efficiency of the hardening processes of the complex structures through the use of the laser fibre mounted on a robotic arm [19–21]. This laser type also presents good electrical efficiency, and virtually maintenance-free [17].

The laser hardening process can affect other properties of the grey cast iron, such as corrosion resistance. The properties of the material can deteriorate with the corrosion process or even, the structures can be destroyed [4,22,23]. In 2022, Fayyadh et al. [23] studied the corrosion resistance of hardened grey cast iron with a CW CO_2 laser (10,600 nm) laser. Laser hardening was carried out in an argon atmosphere and the corrosive environment was 3.5 % wt. NaCl dissolution. The hardness and the corrosion resistance of the iron alloy were improved two times with the laser hardening process. The researchers observed that the microstructural change of the grey cast iron was responsible for the hardness and corrosion resistance increasing on the specimen. Although this study evaluates the corrosion resistance of the materials, this was limited because these analyses only focused on the corrosion rate as determined with a potentiodynamic polarisation curve. The corrosion mechanism evolution, type of corrosion and control of the anodic and cathodic branch were absent in this work. Sai et al. [4] evaluated the mechanical properties and corrosion resistance of grey cast iron

* Corresponding author.
E-mail addresses: j.i.ahuirtorres@ljmu.ac.uk (J.I. Ahuir-Torres), khidly@gtu.ge (N. Bakradze).

https://doi.org/10.1016/j.mtcomm.2025.111852
Received 2 December 2024; Received in revised form 13 January 2025; Accepted 6 February 2025
Available online 7 February 2025

hardened with laser. The research employed the potentiodynamic polarisation curve to assess the corrosion in a saltwater environment. They obtained similar results to those of Fayyadh et al. [23] and also observed the passive film presence on the laser processed samples. The compact laser oxidised layer prevents the chloride anions access to the bared material. Although the controls of the anodic and cathodic branches were studied, the corrosion mechanism evolution over time and type of corrosion were not reported yet.

The corrosion behaviour and mechanical properties of other materials can also benefit from laser hardening. Maharjan et al. [24] investigated the effect of the CW fibre 1070 nm laser hardening on the mechanical properties and corrosion resistance of AISI 4150 steel. Their studies demonstrated that both hardness and corrosion resistance improved as a result of the laser hardening processing. The increase in hardness was attributed to the microstructural change while, the enhancement in corrosion resistance was ascribed to the formation of the chromium oxidise rich layer. Moradi et al. [25] evaluated the Nd: YAG ms pulsed laser hardening effect and laser parameter influence on these properties for AISI 410 steel. They observed that the laser hardening process at low energy fluence improved the corrosion resistance of the samples but reduced their hardness. Conversely, the samples hardened with laser at high energy fluence exhibited greater hardness but lower corrosion resistance. The improved corrosion resistance at low energy fluence was attributed to the retention of the austenitic structure, while the high energy fluence increased the transformation to martensitic structures. Huang et al. [26] assessed the effect of CW Nd: YAG laser hardening and laser power influence on Ti80 alloy properties. The laser hardening process resulted in the increase in the hardness and corrosion resistance of the material. The increase in the hardness was attributed to the refinement of the microstructure while, the enhancement in corrosion resistance was ascribed to the formation of the compact oxidised layer. Among the test conditions, the laser hardened samples at 100 W presented the greatest hardness and corrosion resistance that was attributed to the high degree of the microstructural refinement achieved obtained under this condition.

The literature about laser hardening on cast iron and its mechanical properties is extensive. The corrosion of laser hardened cast iron is scarcely studied, being limited to these few papers. Due to the importance of the corrosion on the structure life time, the present work is focused on the corrosion resistance of laser hardened grey cast iron.

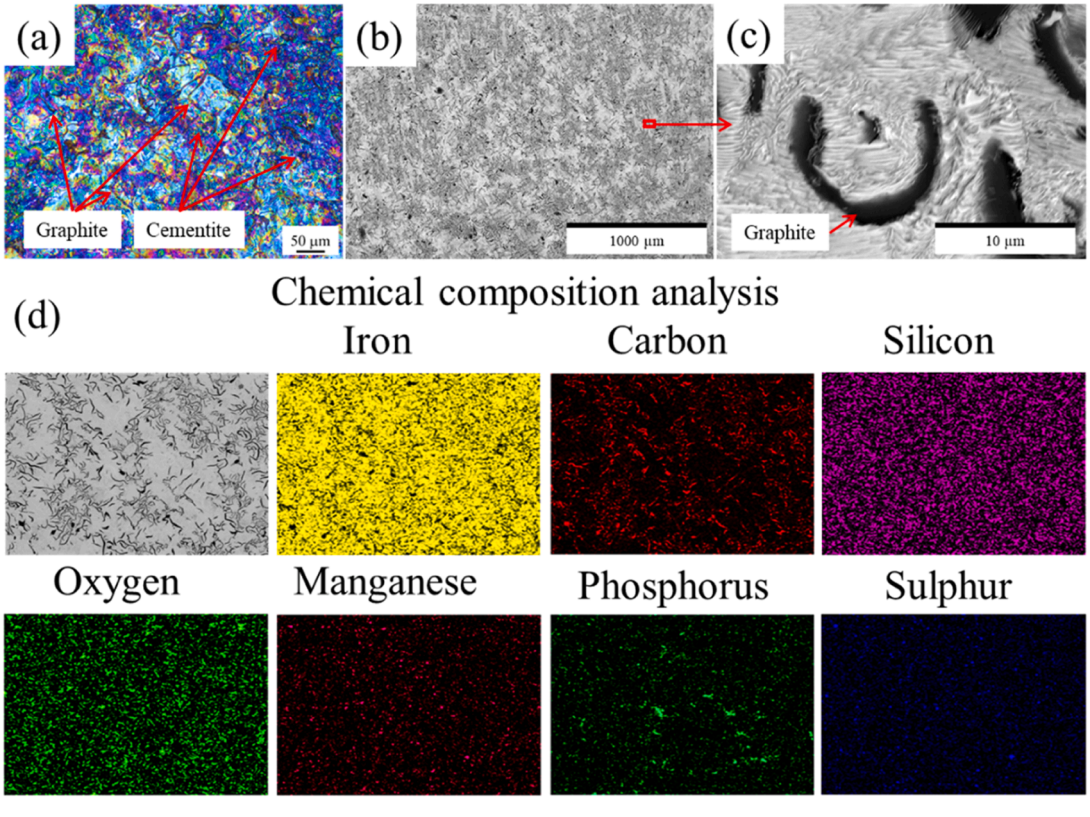

(e)

Zone	Concentration (Atomic%)					
	Fe	C	O	Si	Mn	S
Matrix	53.45	39.94	4.16	2.10	0.33	0.01
Cementite	6.60	90.78	2.21	0.33	0.06	0.02
Graphite	4.80	93.00	1.68	0.38	0.06	-

Fig. 1. Optical digital light microscopy picture (a), scanning electron microscopy pictures with backscattered electrons (b) and (c), energy dispersive spectroscopy mapping (d) and chemical composition (e) of the cast iron microstructure.

2. Experimental setup

2.1. Materials

Samples were commercial grey cast iron with a hypoeutectic interdendritic microstructure with graphite flake (Fig. 1). The pearlite microstructure of the grey cast iron was formed of a α-Fe matrix with cementite (Fe_3C) and flake graphite [1,5,23,27]. The samples were 50 mm in diameter and 3 mm thick.

2.2. Laser equipment

The laser device was an infrared (1070 nm) fibre laser (GSI JK Fibre Laser, model JK400FL) that can work in both continuous wave and pulsed mode (around μs ranges). The specifications of the laser is summarised in Table 1. The laser beam was focused with a focal lens (supplied by Thorlab) of 125 mm focal length.

The focused laser beam (d_o) is estimated with Eq. (1) [28,29] whilst the Rayleigh length is calculated with Eq. (2) [30,31].

$$d_o = \frac{4F_L\lambda M^2}{\pi D_R} \tag{1}$$

$$R_L = \frac{\pi d_o^2}{4M^2\lambda} \tag{2}$$

The specimens were translated under a fixed laser focus using a CNC controlled 3 axes table (Aerotech, UK). The table velocity was from 0.1 mm/s to 5000 mm/s.

2.3. Laser hardening experiments

The laser hardening processes were carried out with two stages but P was 153.3 W, the atmosphere was natural air and the mode was continuous wave for both stages. The first stage aimed to define the laser parameter influence on hardened zone features (size and microstructure). For this reason, the scan speed (SS) and defocused laser beam (D_o) were 1 mm/s, 5 mm/s, 10 mm/s, 20 mm/s and 40 mm/s and, 1 mm, 2 mm, 3 mm and 4 mm, correlatively. D_o was set with the distance from the focal point (Z) using the Eq. (3) [30,31].

$$D_o = d_o\sqrt{1+\left(\frac{Z}{R_L}\right)^2} \tag{3}$$

In the next stage, other specimens were generated with parameters selected in the previous stage and, using several overlapping rates, being 0 %, 25 %, 50 % and 75 %. The overlapping rate (O_R) was calculated with the distance between scans (L) using Eq. (4) [28,32].

$$O_R = 100\frac{W-L}{W} \tag{4}$$

Table 1
IR fibre laser details.

Parameter	Symbol	Value
Mode		Continuous Wave and Pulsed
Wavelength (nm)	λ	1070.0
Power (W)	P	From 0.0–300.0
Transverse Electro Magnetic	TEM	00
Raw beam size (mm)	D_R	6.0
Beam quality	M^2	1.1
Focal length (mm)	F_L	125.0
Focused beam size (μm)*	d_o	32.0
Rayleigh length (μm)*	R_L	650.0
Pulse Length (μs)	τ	From 15–500
Polarisation Orientation	γ	Random

* Data calculated.

2.4. Specimen characterisation

The surface and cross-section of the samples were assessed with digital optical light microscope (Keyence, model VHX-7000) and electron microscope (TM4000Plus, Hitachi). Scanning electron microscopy (SEM) was carried out with backscattered electron, 71 μA current tension, 15 kV potential acceleration and 2 μm spot size. The chemical composition of the specimens was evaluated with energy dispersive spectroscopy (EDS) and the conditions were similar than that for SEM.

The microstructures of the specimens were analysed with the cross section that was polished with the next steps. The first step was grinding with silicon carbide abrasive paper, of grades P200, P400 and P1200. Then, the surfaces were polished with subsequent polycrystalline diamond pastes from 3 μm to 1 μm grain size. The last step was the polishing with colloidal silica gel dissolution of 50 % volume in distilled water and 40 nm grain size. All polishing consumables were provided by Struers. After the polishing process, the cross-sections were etched with nital of 5 % in volume of nitric acid [33].

2.5. Hardness measurement

The Vickers hardness of the samples was measured using a hardness measurement device (Struers, model Duramin). The cross-sections of the laser hardened samples with overlapped scans used to measure the hardness. The load, indentation time and indentation distance were 1 Kg, 10 s and 50 μm, correlatively. Note the ten hardness measurements were carried out on overlapped samples to validate the results.

2.6. Electrochemical testing

Testing was conducted with a potentio/galvanostat (Interface1010E), being handled with Gamry Framework software, and with data analysis performed using Gamry Echem Analyst software. The trials were carried out using three-electrodes cell formed of a 3 M KCl silver/silver chloride (3 M KCl Ag/AgCl) (reference electrode) (EDT directION), a platinum wire with a diameter of 0.7 mm (counter electrode) (Cookson Precious Metlas Ltd) and the sample (working electron). All corrosion evaluations were conducted in 0.6 M NaCl (Merck-Sigma-Aldrich), naturally aerated, at room temperature. The exposed area was set using a tape with a hole and epoxy resin to shield any crevices. The corrosion testing consisted of asymmetrical electrochemical noise, potentiodynamic polarisation curve and electrochemical impedance spectroscopy.

The asymmetrical electrochemical noise (AEN) (non-perturbative test) was conducted with the combination of open circuit potential (OCP) and zero resistance ammeter (ZRA) at the same time. The tests were for 2 hours with 0.05 s acquisition time.

Potentiodynamic polarisation curves (PPC) (perturbative technique of direct current) were conducted with an initial potential was defined on potential at open circuit (for 2 hours of immersion) −0.3 V and potential scan was 0.167 mVs^{-1}, respectively. The current density was limited to 10 $mAcm^{-2}$.

Electrochemical impedance spectroscopy (EIS) (perturbative testing of alternating current) was conducted at 10 mV root mean square (RMS) of potential amplitude, a frequency ranges from 10^{-2} Hz to 10^5 Hz and 10 points per frequency decade. The immersion times in 0.6 M NaCl were conducted at 2 hours, 24 hours, 48 hours, 72 hours and 96 hours of immersion. The equivalent circuit of the EIS data were obtained through Gamry Echem Analyst software to analyse the corrosion mechanism.

To ensure the consistency of results, all electrochemical experiments were conducted at least three times. It is noted that these analyses were conducted on the hardest laser of the hardened samples.

3. Results

3.1. First stage

The laser scans only produced microstructure change with 1 mm/s for all D_o (defocused laser beam diameter) while at 1 mm, the microstructural modification occurred for all *SS* (scan speed). D_o enhancement decreased *SS* that were able to modify the microstructure, being form 1 mm/s to 20 mm/s for 2 mm and form 1 mm/s to 5 mm/s for 3 mm the conditions can change the microstructures (Table 2).

The microstructural change processes require a certain energy density. Energy density (E_d) is defined by *SS* and D_o, Eq. (5) [28,34]:

$$E_d = \frac{P}{SSD_o} \tag{5}$$

Therefore, the increasing of the both parameters (*SS* and D_o) diminishes this energy (E_d), reducing the laser effect on the microstructure.

Most of the laser scanned samples showed two different treated zones in cross-section (Fig. 2 (a)), these being a molten zone (MZ) and a heat affected zone (HAZ). The laser radiation is absorbed at the material surface and transformed in to heat. If E_d is high enough, the material can become molten. This heat is diffused into the material, generating zones with different temperatures that produce solid state microstructural zones, the HAZ [11,13]. In the cases of the laser scans at 4 mm with 1 mm/s and at 3 mm with 5 mm/s, only minimal microstructural changes were observed (Fig. 2 (b)), being similar to HAZ microstructure. If E_d is sufficiently low, the material primarily experiences only moderate heating, limiting the type of microstructural changes [11,28,30].

The MZ microstructure was different to the HAZ microstructure and both were different to the original microstructure (Fig. 3). The MZ microstructure consisted of austenite dendrites with interdendritic ledeburite, without graphite flakes and cementite (Fig. 3 (b)). The carbide elements (cementite and graphite flacks) are re-segregated in melted material [5,11,23]. The HAZ microstructure (Fig. 3 (c)) is a mixture of austenitic and course martensitic with graphite flakes [5,11,23].

The laser treatment clearly modified the chemical composition of the grey cast iron (Fig. 4). The MZ exhibited low concentration of the alloy elements due to the alloy element segregation [11,35]. These elements accumulated in HAZ. The temperature of this region is insufficient to permit the element mobility into the material, producing the massing of these elements [11].

The width (Fig. 5 (a)) and depth (Fig. 5 (b)) of the laser treated zone (LTZ), which formed of HAZ and MZ, and MZ was exponentially decreased with increasing D_o and *SS*. As mentioned, E_d is inversely proportional to D_o and *SS* [8]. The only exception was for 2 mm D_o, where HAZ and MZ was wider than that for 1 mm. This is because width (*W*) also is proportional to D_o and its root, respectively, as showing the Eq. (6) [28,30].

$$W^2 = D_o^2 \ln\left(\frac{E_d}{E_{th}}\right) \tag{6}$$

Where, E_{th} is the minimum energy density required to modify the microstructure.

The laser parameters of D_o 2 mm and *SS* 1 mm/s were selected to carry out the laser hardened samples with overlapping scans (Second stage) because these show two different microstructure (MZ and HAZ) and, MZ *W* was the largest (2 mm). Although D is lower (280 μm) than that for 1 mm (340 μm) at same *SS*, *W* is too larger than for 1 mm (1.2 mm).

3.2. Second stage

The distance between laser scanned zones according to O_R were listed in Table 3. It is noted that the width of the laser treated zone was employed for O_R.

Fig. 6 showed the cross-sections of the overlapped laser scanned samples where MZ and HAZ were also observed. The microstructures of both zones were similar to them seen in single laser scanned samples.

MZ and HAZ were deeper with the increase of the overlapping as can be seen in Table 4. The laser energy is accumulated in each laser scan and is diffused into the samples, enlarging the size of the laser hardened zone [36].

MZ and HAZ of all overlapped laser scanned samples were harder than the non-laser processed specimens (Fig. 7). The martensitic microstructure is harder than hypoeutectic interdendritic microstructure [5,10]. MZ was harder than HAZ as a result of the austenitic microstructure and graphite flakes that weaken the martensitic microstructure. The hardest specimen was the laser hardened samples at 25 % overlapping. MZ hardness of this sample was 850 $HV_{1\ kg}$ while HAZ was similar than other laser hardened samples. It is important to highlight that the MZ of the laser hardened samples with 25 % overlap (850 HV) exhibited greater hardness compared to the grey cast iron treated using quenching (800 HV [37]), high energy electron beam irradiation (800 HV [38]) and surface heating (700 HV [39]). The residual compression stresses and dislocations accumulated with the laser scan overlapping harden the material [36]. An excessive overlapping can however generate microcracks, reducing the hardness of the material [28,40].

3.3. Electrochemical analyses

3.3.1. AEN analyses

Both AEN signals (potential-OCP and current density-ZRA) of both samples fluctuated over the time (Fig. 8) due to the metastable micropitting generation [41–43]. The voltage in both cases (Fig. 8 (a)) decreased over the time. This can indicate the chemical activation of the sample as a result of the oxidised layer dissolution in water [44]. The laser hardened sample potential was larger than as-received specimens, showing the nobler of the hardened specimen. Laser oxidised layers usually are nobler than native oxidised layer due to more extensive

Table 2
Efficient laser parameters.

	Scan speed (mm/s)				
Laser beam diameter (mm)	1	5	10	20	40
1	■	■	■	■	■
2	■	■	■	■	
3	■	■			
4	■				

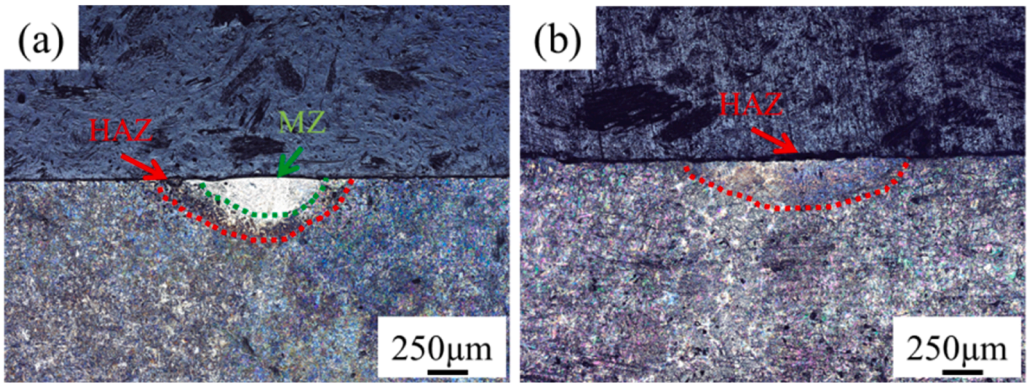

Fig. 2. Cross-section optical digital light microscopy pictures of the laser scanned material at 5 mm/s with 1 mm (a) and 3 mm (b).

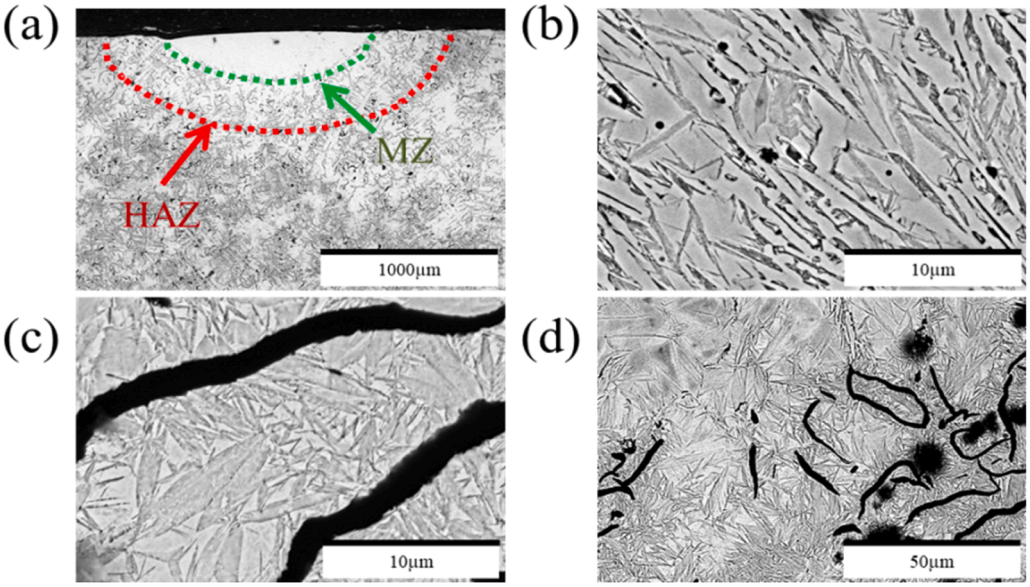

Fig. 3. Cross-section SEM pictures of the full (a), MZ (b), HAZ (c), and zone between HAZ and MZ (d) of the laser scanned material at 1 mm/s with 1 mm.

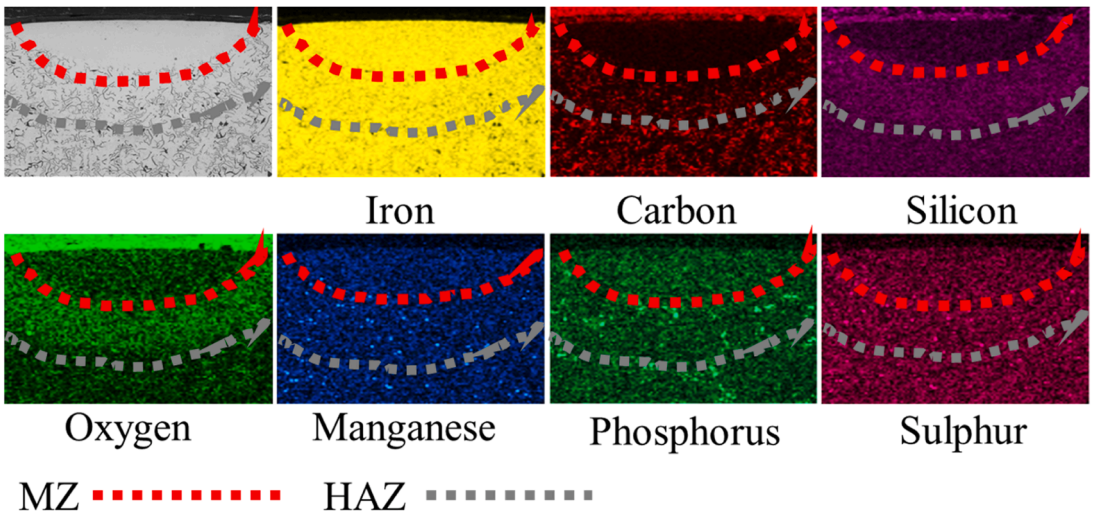

Fig. 4. EDS mapping of the laser hardened samples cross-section with 1 mm/s, 1 mm and 153.3 W.

oxidation [4,23]. The laser hardened sample microstructure also displayed increased nobility [45]. Current density evolution over time (Fig. 8 (b)) was dissimilar according to the sample. In the case of the laser hardened samples, the current density increased with time, confirming the chemical activation of the specimens. In respect of the as-received samples, the current density was also increased with time for

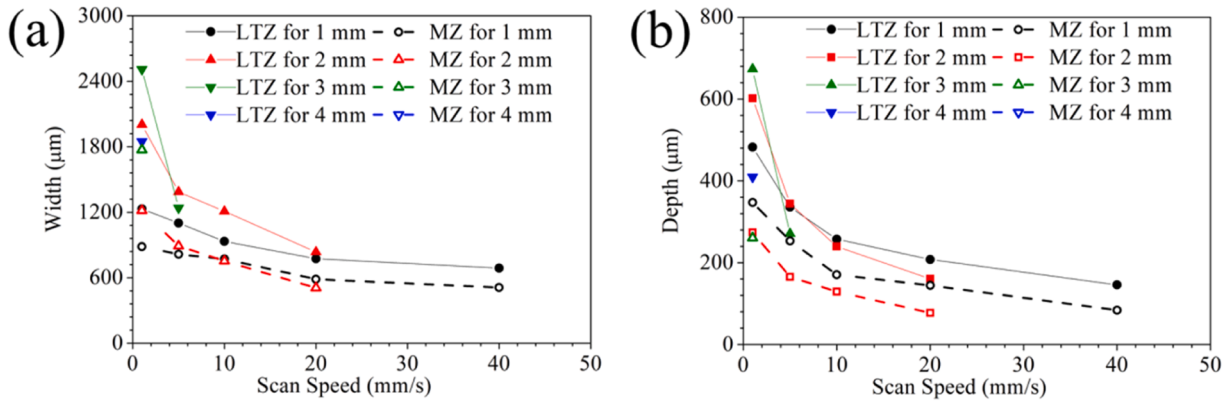

Fig. 5. Width (a) and depth (b) of the LTZ and MZ according to the D_o and SS.

Table 3
Summary of the distance between laser scanned zones according to O_R.

Overlapping Rate (%)	0	25	50	75
Distance between laser scanned zones (μm)	2000	1500	1000	500

immersion times lower than 2800 s. The current density was however diminished with time for 2800 s or longer immersion time. At ≤ 2800 s, the corrosion products are dissolved in the water. After (> 2800 s), the corrosion products are deposited and produced on the surface, generating an oxidised layer that diminishes the corrosion [46].

The features of the corrosion process obtained with AEN results were summarised in Table 5. The charge density (Q) was figured with quick integral [42] while asymmetric electrochemical noise resistance (R_{AEN}) was calculated with the Eq. (7) [47].

$$R_{AEN} = \frac{\sigma_E}{\sigma_I} \tag{7}$$

where, the standard deviation of the potential and current density are σ_E and σ_I. The kinetic parameters of the corrosion as Q, root mean square current density ($I_{R.M.S}$) and R_{AEN}, were slightly lower for the laser hardened samples than as-received specimens. This indicates the higher corrosion resistance of the laser hardened samples in the kinetic aspect.

Localised index (*L.I*) indicates the type of corrosion and is estimated with Eq. (8) [44,47].

Table 4
MZ and HAZ depth according to O_R.

O_R (%)	MZ depth (μm)	HAZ depth (μm)
0	280	600
25	300	850
50	470	1120
75	520	1300

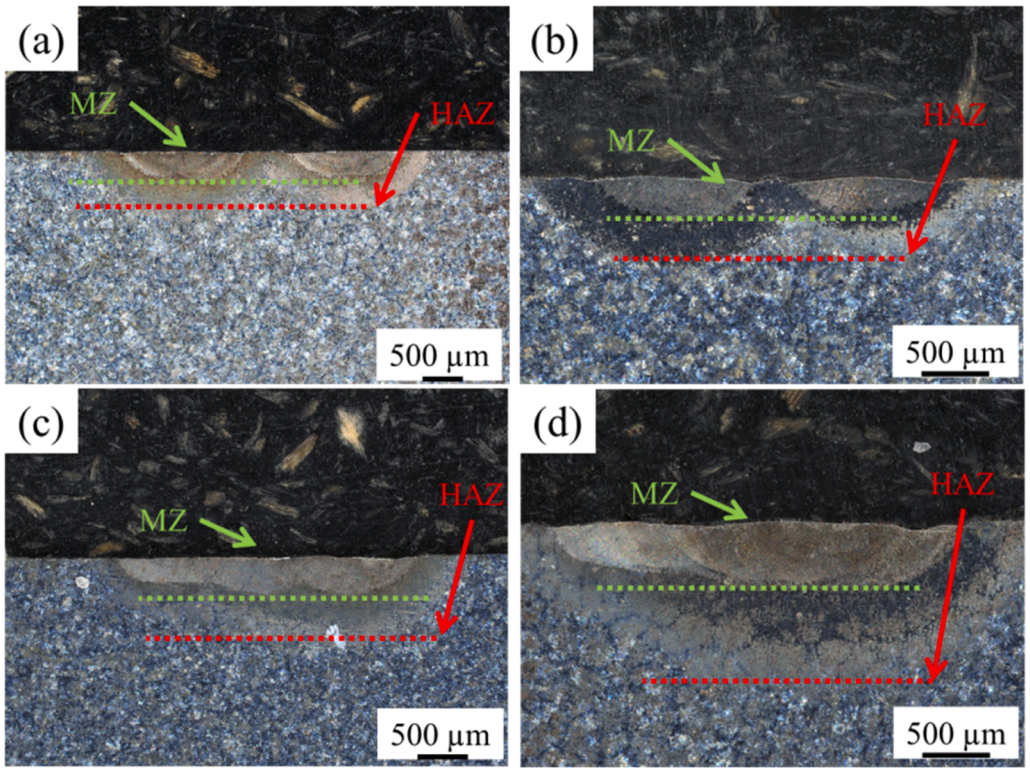

Fig. 6. Laser scanned samples with 0 % (a), 25 % (b), 50 % (c) and 75 % (d) overlapping.

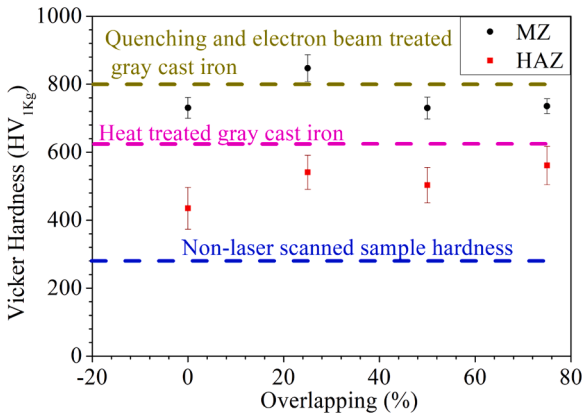

Fig. 7. Graph of the laser processed samples hardness according to the overlapping and, hardness of the quenched [37], high energy electron beam irradiated [38] and heat treated [39] grey cast iron.

$$L.I. = \frac{\sigma_I}{I_{R.M.S}} \quad (8)$$

L.I. values showed that the corrosion kind of the samples were similar for each other, being mixed corrosion (localised and general) (from >0.01 to ≤0.1) [44].

3.3.2. PPC assessments

Although PPC shape was different according to the samples (Fig. 9), both samples had a vertical curve at the lowest potential (-0.960 V). This signal is due to the water evolution generated [48].

The cathodic branch was a tilted curve for the as-received specimen, showing an activation control of the reduction reaction [49]. The curve shape changed with the potential on the anodic branch. The curve was vertical from −0.750 V to −0.655 V, indicating passivation control [4]. At higher potential than −0.655 V, the curve was horizontal. The dramatic increment of the current density with the potential indicates pitting generation [4,48,50].

The curve of the laser hardened samples was vertical in the cathodic branch, indicating a diffusion control of the reduction reaction [49,51]. The tilted curve in the anodic branch shows an activation control of the oxidation reaction [49].

In both cases, the chemical reactions for the anodic and cathodic reaction were the [43,52].

$Fe \rightarrow Fe^{+3} + 3e^{-}$ (anodic)

$2H_2O + O_2 + 4e^{-} \rightarrow 4(OH)^{-}$ (cathodic)

Table 6 summarised the thermodynamic and kinetic characteristics of the corrosion measured with PPC.

The thermodynamic corrosion resistance was the corrosion potential (E_{corr}) that was figured as the potential where both branches matched. The laser hardened samples had the highest E_{corr}, validating an increase of the nobility with laser hardening [53]. The homogenisation of the microstructure [45] and the laser oxidised layer [4,23] increase the corrosion potential. The breaking semi-passive film (E_{bsp}) was the voltage in the anodic branch where current density increased with increasing potential. This potential was absent for the laser hardened samples because the laser oxidised layer possesses breaking semi-passive film potential similar to corrosion potential [48]. Despite this handicap, laser hardened sample presented better thermodynamic corrosion

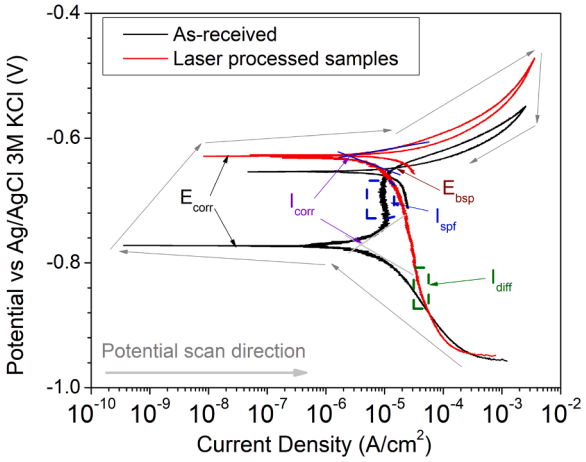

Fig. 9. PPC of the as-received and laser hardened (2 mm, 1 mm/s, 153.3 W and 25 % overlapping) samples in 0.6 M NaCl.

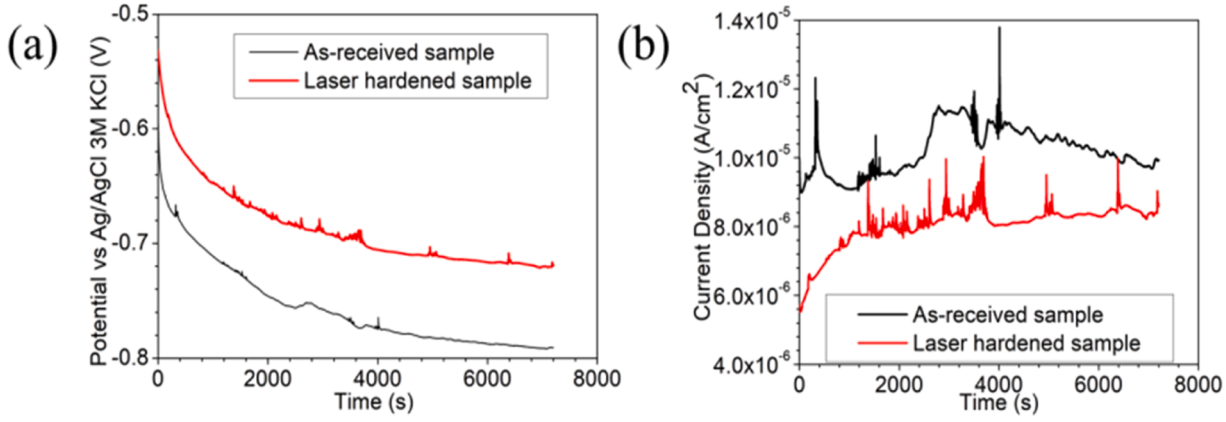

Fig. 8. OCP (a) and ZRA (b) of the as-received and laser hardened (2 mm, 1 mm/s, 153.3 W and 25 %) samples in 0.6 M NaCl.

Table 5
Samples corrosion features gotten with AEN analyses.

Sample	Q ($mCcm^{-2}$)	$I_{R.M.S}$ (μAcm^{-2})	σ_E (mV)	σ_I ($nAcm^{-2}$)	R_{AEN} ($K\Omega cm^2$)	L.I
As-received	73	10	36	667	54	0.06
Laser hardened	58	8	35	596	60	0.07

Table 6
Samples corrosion features obtained via PPC assessment.

	As-received Sample	Laser Hardened Sample
E_{corr} (V)	−0.775	−0.625
I_{corr} (μAcm^{-2})	8	5
β_c (AV^{-1})	−0.037	−0.039
β_a (AV^{-1})	0.033	0.035
R_p (KΩcm^{-2})	20	26
E_{bsp} (V)	−0.655	-
I_{bsp} (μAcm^{-2})	10	-
I_{diff} (μAcm^{-2})	-	32

resistance than the as-received sample owing to its E_{corr} was higher than E_{bsp}. This means that laser hardening generates grey cast iron nobler than semi-passive film [53]. Note that the return curve of the as-received samples coincided with the forward curve at higher potential than E_{corr}. This shows that the semi-passive film can spontaneously recover [54]. It is emphasised that the current density of the semi-passive film (I_{bsp}) was 10^{-5} Acm^{-2}. The passive film has current densities of 10^{-6} Acm^{-2} or lower [50]. Therefore, this protective film cannot be considered as passive film.

The kinetic corrosion characteristics were corrosion current density (I_{corr}) and polarisation resistance (R_p) for both samples. I_{corr} was calculated with the extrapolation of the Tafle lines [51] and R_p with the Eq. (9) [43,47].

$$R_p = \frac{\beta_a \beta_c}{2.303 I_{corr}(\beta_a + \beta_c)} \quad (9)$$

The laser hardened sample R_p was slightly higher than that for as-received specimens. Other kinetic characteristics, as semi-passive film current density (I_{spf}) for as-received sample and the diffusion current density (I_{diff}) for laser hardened samples, were similar for each other. I_{spf} was figured in the vertical curve of the anodic branch while I_{diff} was measured in the cathodic branch vertical curve.

3.3.3. EIS assessments

The evolution of the corrosion mechanism over the time in 0.6 M NaCl was observed in Nyquist and Bode plots (Fig. 10). The equivalent circuit method was used to analyse the corrosion mechanism of the sample according to the immersion time. All equivalent circuits can be seen in Fig. 11. Albeit, all samples at all immersion time had a horizontal curve at high frequency range (F) (from 10^3 Hz to 10^5 Hz) in the Bode plots of F vs impedance modulus (Z_m), showing the resistance presence (R_1) [55].

As-received samples possessed two positive semi-loops in Nyquist plots for first two immersion hours, indicating the presence of two time constants. The time constants are formed of one constant phase element (CPE_2 and CPE_3) in parallel with a resistance (R_2 and R_3) in both time constant [56]. In the Bode plots, these time constants were observed as tilted curves with dissimilar slope for Z_m vs F and as two peaks for phase angle (P) vs F [57]. The overlapping of the peaks (P vs F) shows that R_2 was in serial with CPE_3 [48]. A negative loop was observed in all Nyquist plots, showing the adsorption-desorption process [57,58]. This was validated by the inclined curve with negative slope at low frequency range (from 10^{-2} Hz to 10^{-1} Hz) for Z_m vs F plots [56]. This was represented as CPE_4 with negative n and, which is in serial with R_3. The equivalent circuit to represent this corrosion mechanism can be seen in Fig. 11 (a). Note that these results were observed in the literature [59] but the corrosion mechanism was not discussed in depth. After 24 hours of the immersion, the corrosion mechanism of the as-received specimen showed an evolution in the negative loop. This was only localised at high real impedance in the Nyquist plots and a tilted curve with negative slope was absent. This means the presence of a resistance (R_4) in parallel with CPE_4 [56]. R_4 is besides associated with adsorption-desorption process. A schematic drawing of this equivalent circuit can be found in Fig. 11 (b). At 48 hours of immersion, the corrosion mechanism evolved again where R_4 and CPE_4 were replaced by an inductor (L) that represented the same process. L was in parallel with other time constants. The absence of the negative loop was signal to this evolution. Fig. 11 (c) is the sketch of the equivalent circuit, which was also used to represent the corrosion mechanism for 72 hours of immersion. The last evolution of the corrosion mechanism was at 96 hours and this was characterised by the tilted curve at low frequency range (from 10^{-2} HZ to 10^{-1} Hz) in Z_m vs F. This is characteristic of the impedance due to the mass transport process (diffusion). Warburg impedance (W) is typically employed to represent this process in the equivalent circuit [55,56,60]. W replaced to L and was in serial with R_3 (Fig. 11 (d)).

In the case of the laser hardened samples (Fig. 10 (b)), the equivalent

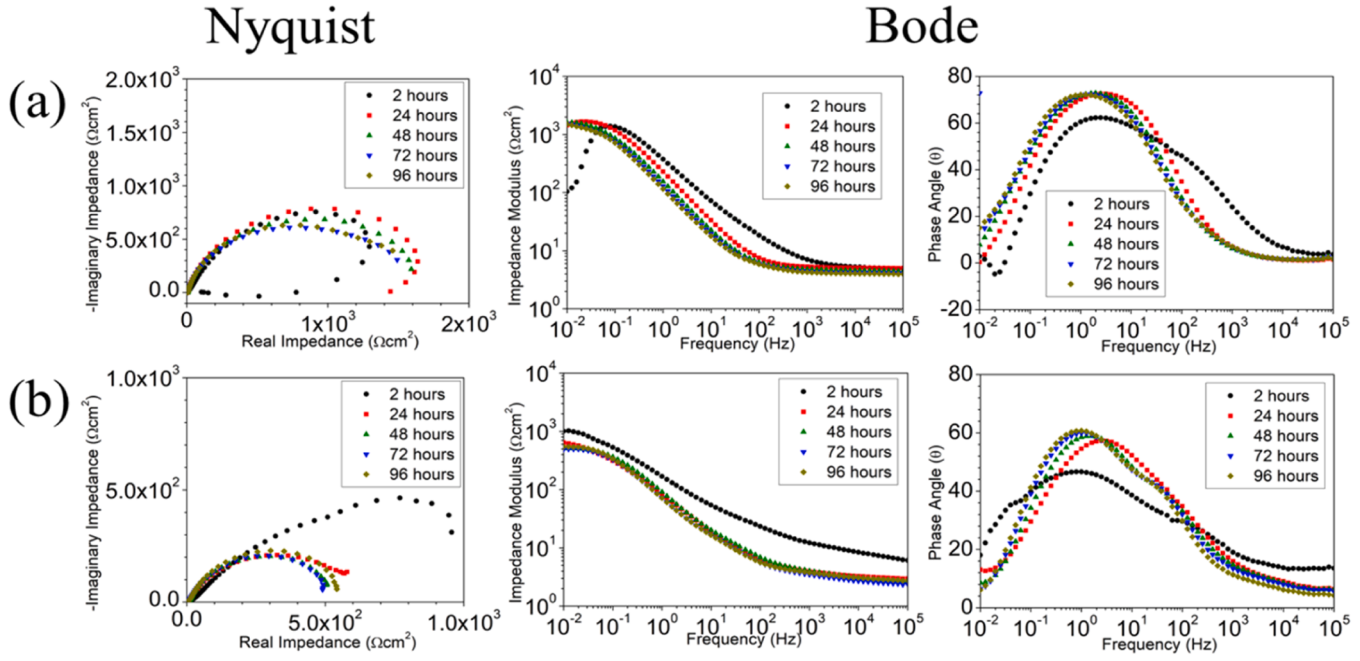

Fig. 10. EIS of the as-received (a) and laser hardened (2 mm, 1 mm/s, 153.3 W and 25 % overlapping) (b) samples in 0.6 M NaCl.

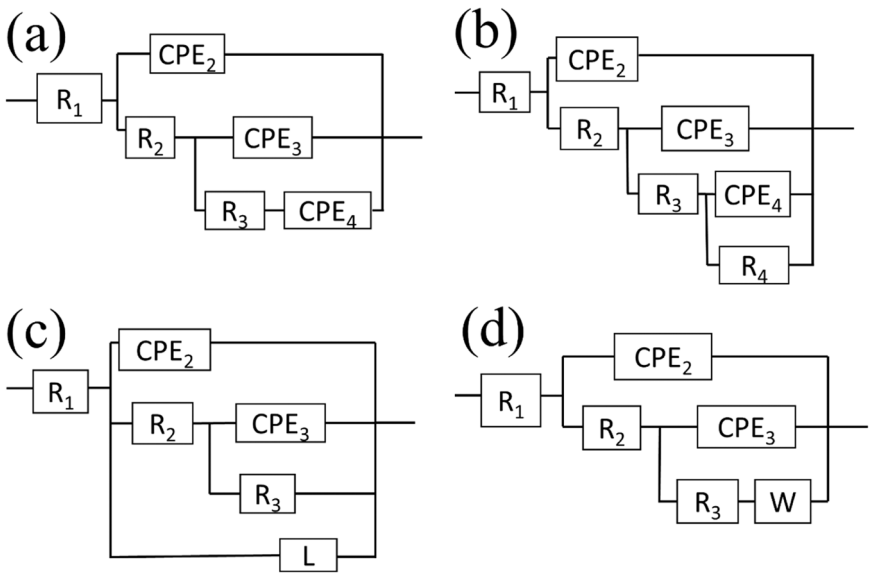

Fig. 11. First (a), second (b), third (c) and fourth (d) equivalent circuits to represent the corrosion mechanism of the specimens in 0.6 M NaCl at various immersion times.

circuit of the as-received specimen at 96 hours was used for the most of the immersion times (Fig. 11 (d)). The only exception was at 2 hours of immersion where the equivalent circuit was Fig. 11 (b). It is noted that the R_4 and CPE_4 can represent different process than that for as-received sample. This is due to the dissimilar signals of the Nyquist and Bode plots. An extra loop at high real impedance for Nyquist plots, an inclined curve and an extra peak at low frequency range (from 10^{-2} Hz to 10^{-1} Hz) for the Bode plots (Z_m vs F and P vs F respectively) were the signal for this time constant [56].

Table 7 summarises the values of the equivalent circuit elements. The good chi-square values ($\approx 10^{-4}$) confirmed the validation of the equivalent circuit to represent the corrosion mechanism of the specimens. R_1 was remained constant over the time, meaning that this represents the dissolution process [61].

The second constant time elements (R_2, CPE_2 and n_2) also were constant with time for the as-received samples, showing the stability of this corrosion process over time [57]. It is noted that n_2 had values lower 1 ($\approx$ 0.7–0.8), indicating a surface imperfection such as roughness [62]. Similar behaviour was observed for the laser hardened specimen second time constant. The only exception was n_2 that was increased from 0.43 to 0.74 for immersion times from 2 hours to 48 hours. This can be due to a flattening process on the surface during the saltwater immersion. For immersion times longer than 48 hours, n_2 was remained constant over the time. The second constant time elements possessed similar values for both samples for each immersion time. These results show that this element of the corrosion mechanisms is more or less stable over time.

The third constant time elements had an evolution over time stronger than the elements of the second constant time for both specimens. As received sample R_3 was decreased from 2 hours to 24 hours. After, this was increased at 48 hours and finally, was reduced again with the time for 72 hour of immersion or more. CPE_3 of the same sample was diminished form 2 hours to 24 hours. Then, this element was increased over the time for $\geq$ 48 hours. n_3 was increased with the immersion times for 24 hours or less from 0.54 (2 hours) to 0.92 (24 hours). This then remained constant over time. According to this data, this element's features fluctuated over time, increasing and reducing the corrosion resistance, the thickness and, surface quality. The resistance is part of the sample corrosion resistance [59]. The thickness of the element is proportional to the CPE [57,60]. Roughness [61] and dielectric relaxation [63] is inversely proportional to n. In the case of the laser hardened samples, the three elements of the third constant time increased with time for immersion times shorter than 24 hours. For times greater than 48 hours, the values fluctuated over time. The corrosion resistance increase can be followed by the improvement of the surface quality with a thinning of the thickness for the first immersion hours. Later, the element of the corrosion mechanism can remain in dynamic

Table 7
Samples corrosion mechanism features get with EIS.

As-received Sample													
Time (h)	R_1 (Ωcm^2)	R_2 (Ωcm^2)	CPE_2 ($mSs^n cm^{-2}$)	n_2	R_3 (Ωcm^2)	CPE_3 ($mSs^n cm^{-2}$)	n_3	R_4 (Ωcm^2)	CPE_4 ($mSs^n cm^{-2}$)	n_4	L (Hcm^2)	W ($Ss^{0.5} cm^{-2}$)	χ^2 (10^{-4})
2	5.071	5.675	0.963	0.71	323	2.320	0.54	-	62.500	−4.0	-	-	85
24	2.864	3.108	1.320	0.84	35	0.274	0.92	1670	0.314	−0.2	-	-	6
48	4.567	4.181	0.895	0.86	1736	0.461	0.87	-	-	-	10800	-	2
72	4.181	6.571	1.320	0.82	1642	0.378	0.91	-	-	-	27500	-	2
96	4.062	5.282	0.850	0.87	1532	0.848	0.87	-	-	-	-	0.044	2
Laser Hardened Sample													
Time (h)	R_1 (Ωcm^2)	R_2 (Ωcm^2)	CPE_2 ($mSs^n cm^{-2}$)	n_2	R_3 (Ωcm^2)	CPE_3 ($mSs^n cm^{-2}$)	n_3	R_4 (Ωcm^2)	CPE_4 ($mSs^n cm^{-2}$)	n_4	L (Hcm^2)	W ($Ss^{0.5} cm^{-2}$)	χ^2 (10^{-4})
2	3.345	9.513	0.846	0.43	50	0.407	0.69	1800	0.834	0.68	-	-	9
24	4.648	3.242	0.334	0.69	1330	1.560	0.73	-	-	-	-	0.114	10
48	4.522	2.504	0.396	0.74	1023	1.830	0.81	-	-	-	-	3.340	11
72	3.854	2.156	0.494	0.78	1223	2.080	0.85	-	-	-	-	2.340	9
96	3.705	2.256	0.548	0.77	1184	2.330	0.85	-	-	-	-	0.227	8

equilibrium. This can be due to the different equivalent circuit for 2 hours than for longer immersion times. It is possible that the fourth time constant of the 2 hours equivalent circuit represents the same corrosion mechanisms element than the third time constant of the greater than 24 hours equivalent circuit. In this case, the time constant elements only fluctuated over time.

3.4. Corroded samples surface evaluation

As received samples exhibit large cracks on the surface (Fig. 12 (a)) that revealed the internal pearlite microstructure. The cross-section of the samples (Fig. 12 (c)) showed that some graphite flakes were removed, generating corroded cracks where the corrosion products were amassed. The graphite presents a cathodic effect on the α-Fe matrix due to the high potential difference between these. This provokes that the iron around the graphite is corroded, prompting the dissolution on water. When the most of the iron matrix has been dissolved, the graphite flakes detached, generating the groove [43,64].

In contrast, the laser hardened samples possessed a homogeneous corroded surface with microcracks and micro-pitting (Fig. 12 (b)). The oxidised layer was homogeneous and porous without large groove (Fig. 12 (d)). The absence of the graphite flakes decreases the cathodic effect and the production of large cracks or grooves. White flaky particles were seen on the surface of these samples (Fig. 12 (b)). These can be crystals of FeOOH as mentioned by Guo et al. [65].

EDS mapping analyses of the corroded samples with PPC (Fig. 13) showed different chemical composition according to the specimen. In both sample surface (Fig. 13 (a-b)), the light particles were formed from the metallic elements of the alloy (iron, manganese and sulphur). The localised dissolution of the oxidised layer exposes the internal material. The as-received surface (Fig. 13 (a)) and cross-section (Fig. 13 (c)) had a heterogeneous distribution of the alloy elements. High oxygen concentration was observed around the graphite flakes. The cathodic effect of the graphite flakes prompts the corrosion of the iron matrix [53]. This was also observed in the cross-section of the as-received sample (Fig. 13 (c)), meaning the corrosion followed the graphite in depth. This generated an oxidised layer with heterogeneous thickness. The laser hardened specimens (Fig. 13 (b) and (d)) possessed a more homogeneous oxidised layer in chemical composition. The refining of the microstructure reduces or eliminates the cathodic effect of the graphite flakes [53]. Some localised damage was observed due to the affinity of the Fe(OOH) to the chlorine anion. $FeCl_3$ can be dissolved in water, producing the oxidised layer damage [65].

4. Discussion

Laser hardening samples can be designed with the correct combination of laser parameters. The laser scanning with low E_d (fast *SS* scan and large D_o) only had one microstructural modified area while laser scanning with high energy density (slow *SS* and small D_o) offered more parameter sets with microstructural modification. High E_d can melt the cast iron and generates a heat affected zone HAZ around the MZ. The material can only be heated at low E_d, producing HAZ by solid state transformation [11,28,30]. MZ exhibited austenite dendrites with interdendritic ledeburite and with an absence of graphite flakes. The quick melting and cooling of the material permit can create metastable microstructures because the material has insufficient time to come back to stable status [5,11,23]. The enrichment in iron of the region also encourages the metastable microstructure formation. The melting prompts the segregation of the light alloy element (e.g., carbon, oxygen and silicon) [11,35], producing the iron enriching. The HAZ presented austenitic and coarse martensitic microstructure with graphite flacks. The temperature increase was insufficient to refine the microstructure. The segregated alloy elements also were accumulated in the HAZ, encouraging this microstructure [11,28,30]. The size of the laser treated zone was moreover influenced by the laser parameters. The width and depth are proportional to energy density due to the Gaussian energy spatial distribution [8,11,28,30]. Width and depth besides are proportional to laser beam diameter [28,30] and laser - material interaction time [8,11].

All samples treated with overlapping scans showed an increase in hardness compared to the as-received sample. The new microstructures and the thermal stresses increase the hardness of the material. The hardness is intrinsically related with the microstructure due to the tensions and stress produced in each one [30]. MZ was harder than HAZ owing to the dissimilar microstructure and thermal stresses. Austenite dendrites with interdendritic ledeburite is harder than austenitic and coarse martensitic microstructure with graphite flacks. HAZ reaches lower temperatures than MZ, which produces low stress number and weaker [5,10]. The samples with 25 % overlapping however exhibited the highest hardness. The magnitude of thermal stress is proportional to the overlapping of the laser scan [36]. Low overlapping produces a lower stress than higher overlapping. When the magnitude of the thermal stress is too high, cracks are produced due to an excessive tension

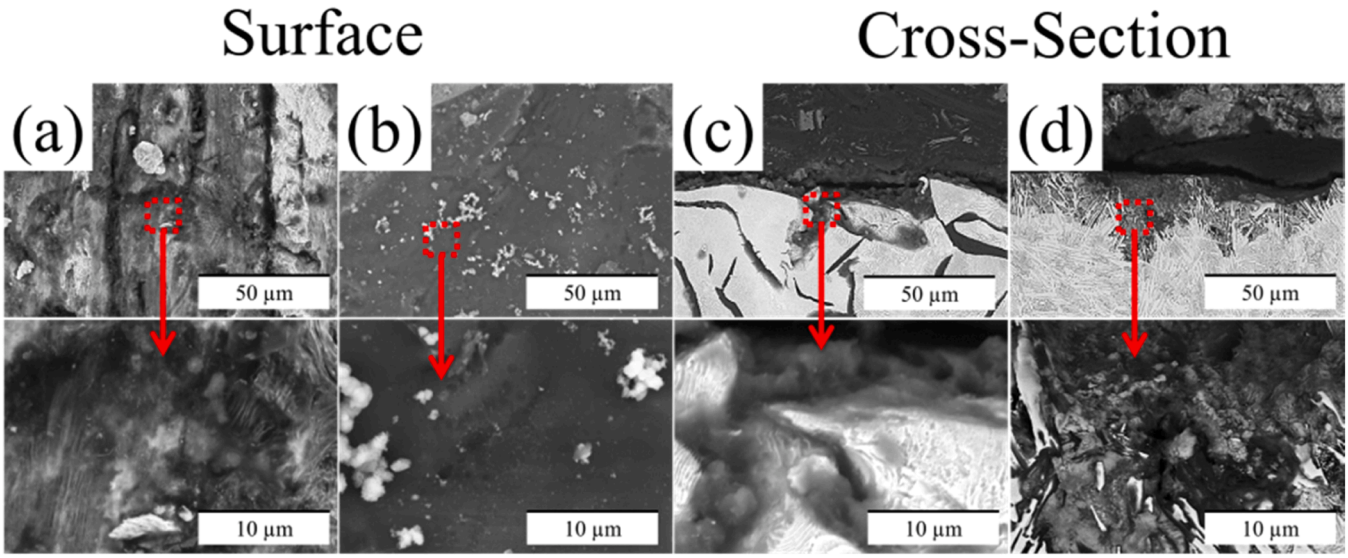

Fig. 12. SEM pictures with backscattered electrons of the surface (a-b) and cross-section (c-d) of the corroded as-received (a) and (c) and laser hardened specimens (b)and (d) with PPC in 0.6 M NaCl.

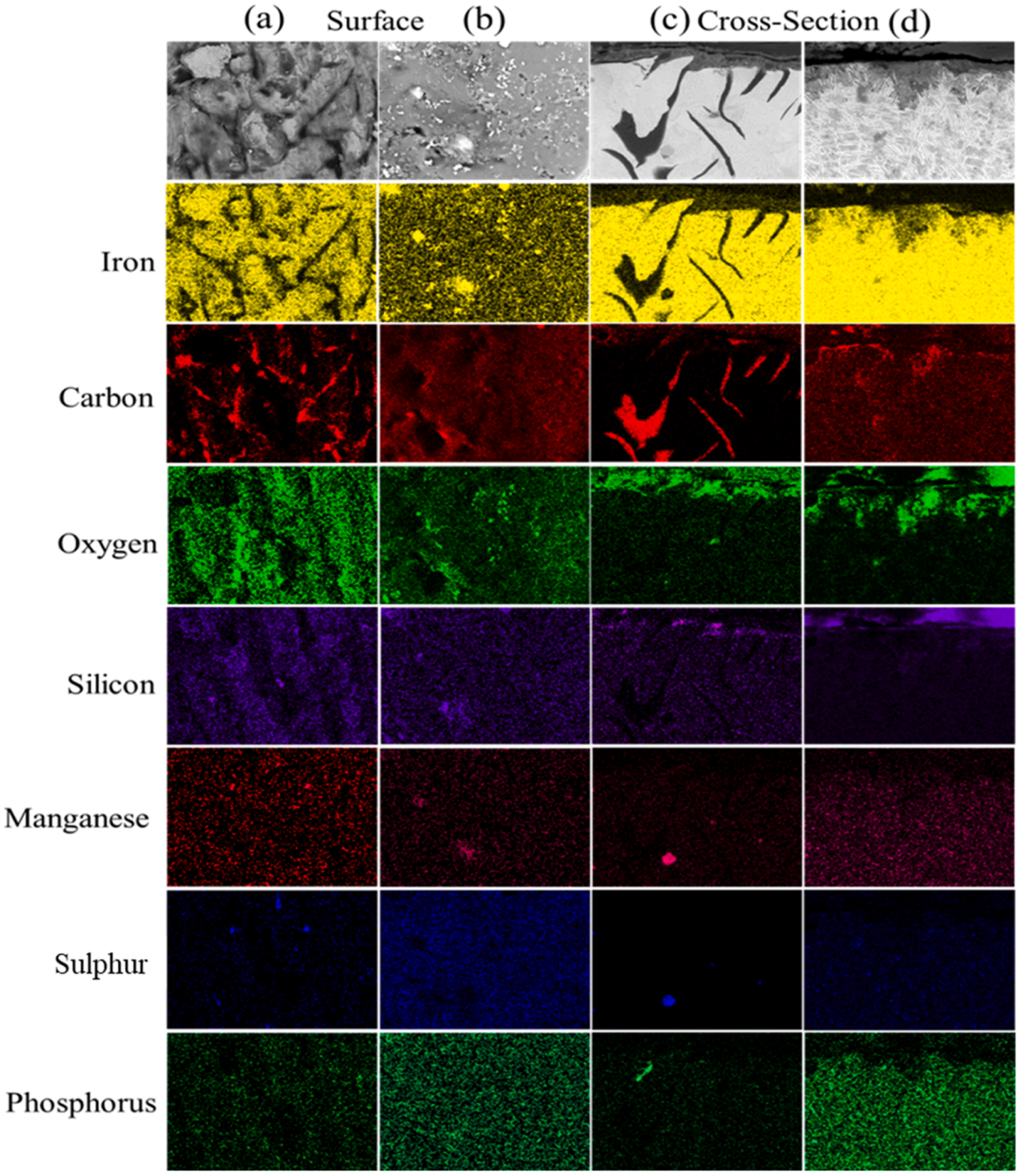

Fig. 13. EDS mapping of the surface (a-b) and cross-section (c-d) of the corroded as-received (a) and (c) and laser hardened specimens (b) and (d) with PPC in 0.6 M NaCl.

into the material [28,40].

The laser hardening process with overlapping laser scan at 25 % also showed better corrosion resistance than as-received samples. This was confirmed by the higher polarisation resistance (R_p) for laser hardened sample than for as-received sample. The corrosion rate is proportional to these resistances [43,47]. R_p was similar to asymmetric electrochemical noise resistance (R_{AEN}), validating the results. Although the passive region was absent for the laser hardened samples potentiodynamic polarisation curve (PPC), the E_{corr} of the samples was higher than E_{bsp}. This indicates that the oxidised layer generated with laser is nobler than native oxidised layer [53]. The corrosion potential of the austenite dendrites with interdendritic ledeburite microstructure is similar to its breaking semi-passive layer potential, eliminating the passive region in PPC [53]. Another difference in PPC was the cathodic branch that was controlled by activation and diffusion for as-received and laser hardened samples, respectively. The roughness topography of the laser hardened sample causes diffusion impedance. The relief hinders the access of the liquid to the samples, producing the accumulation of the oxygen and the water in the chemical active area, giving an impedance.

The corrosion mechanisms evolved over time with different behaviour according to the sample (Fig. 14). Albeit, R_1 corresponded to the solution resistance (R_s) [60] for both samples at all immersion time.

The corrosion mechanism at 2 hours of immersion for as-received material (Fig. 14 (a)) consisted of the oxidised layer, chlorine adsorption-desorption and bared material process. The second time constant of the first equivalent is associated to oxidised layer process (R_2/R_{OL} and CPE_2/CPE_{OL}) while bared material is represented by third constant time (R_3/R_{ct} and CPE_3/CPE_{dl}). The resistances represent the charge transference resistance of the metallic material to environment [43,65]. CPEs render the double layer formed by charge alignment between the alloy and the environment [43]. The negative value of n_4 indicates CPE_4 corresponded to adsorption/desorption process ($CPE_{ad\text{-}de}$). The high affinity of the iron to hydroxide anions produces the adsorption-desorption process [46] that is encouraged by the cathodic effect of graphite flakes. This initial adsorption-desorption processes were also observed in low values of n_{dl} (0.69). The dielectric relaxations of the samples can be correlated to these low values [63]. With time (24 hours of immersion), the chlorine ions adsorbed are accumulated on the surface, generating a resistance to the adsorption-desorption process ($R_4/R_{ad\text{-}de}$). This also removes the charge relaxation effect as can be seen value increment of n_{dl} (≈1.00). The amassing of adsorbed chlorine anions also encourages the charge transference from the bared material to water as can be seen in R_{ct} reduction. Thus, the corrosion mechanism for this immersion time consisted of the same processes but these are represented with other elements. After (from 48 hours to 72 hours), the iron matrix around graphite flakes dissolve. The cathodic effect of the graphite flakes promote this dissolving process [43,64]. This dissolution enlarges the contact area of the samples with the water, removing the accumulation of chlorine ions on the surface. This causes that $R_{ad\text{-}de}$ is absent for equivalent circuit between 48 hours and 72 hours. $CPE_{ad\text{-}de}$ was replaced by $L_{ad\text{-}de}$ as a result of the weakening of the adsorption-desorption process. The graphite flakes can be degraded in water environment, diminishing their cathodic effect on iron matrix. This, in turn, decreases the adsorption-desorption process [43,64]. The weakening of the adsorption-desorption process also produces the R_{ct} increase. Again, the processes of the corrosion mechanism are the same represented with different elements (W). At the longest immersion time (96 hours), the graphite flakes were detached from the grey cast iron surface. When totality of the iron is dissolved in water, the graphite is cast off. This detachment produces the elimination of the adsorption-desorption process. The cathodic effect is stopped with the graphite removal [43,64]. This detaching generates cracks that produced Warburg or diffusion impedance (W). The cracks and pores hinder the water and oxygen access to the bared material [66]. Therefore, the processes of the corrosion mechanisms at 96 hours were oxidised layer, diffusion and bared material processes.

The corrosion mechanism evolution of the laser hardened samples with overlapped scans at 25 % (Fig. 14 (b)) was only produced between 2 hours and 24 hours of immersion. At 2 hours of immersion or less, the corrosion mechanism was comprised of the laser oxidised layer, oxidised layer and bared material. The second time constant (R_2, n_2 and CPE_2) represented the laser oxidised layer process (R_{LOL}, n_{LOL} and CPE_{LOL}) in this case. The continuous-wave laser hardening in air atmosphere produces the thermal oxidation of the metallic material [28]. The oxidised layer process (R_{OL}, n_{OL} and CPE_{OL}) was rendered with the third time constant (R_3, n_3 and CPE_3). The last time constant (R_4, n_4 and CPE_4) represented the bared material process (R_{ct}, n_{dl} and CPE_{dl}). The low values of n_{dl} (0.68) is also dielectric relaxation process [63] while n_{LOL} (0.49) and n_{OL}.(0.69) values are due to the high surface roughness created with the laser [62]. The laser oxidised layer process was absent for the corrosion mechanism at 24 hours or more of immersion owing to the dissolution in water of this element. The dissolution provokes microcracks that cause diffusion impedance [66]. Thus, the corrosion mechanism was formed of oxidised layer (R_{OL}, n_{OL} and CPE_{OL}), bared material (R_{ct}, n_{dl} and CPE_{dl}) and diffusion impedance (W) process, being represented by second (R_2, n_2 and CPE_2) and third (R_3, n_3 and CPE_3) time constant, and Warburg impedance (W), respectively. It is noted that n_{OL} and n_{dl} was increased at values close to one for immersion time of 24 hours or more. The deposition of the corrosion products on the surface can smooth the surface.

The higher stability of the laser hardened samples over the time is due to the microstructural refining that removes the graphite flakes. These particles encourage the adsorption-desorption process and the dissolution of the material [43,64]. This causes a process of the graphite flakes elimination, provoking dramatic evolutions with time. The high density of the laser oxidised layer also improves the corrosion resistance of the material [4,23].

5. Conclusions

This work about the improvement of the grey cast iron hardness and corrosion resistance has delivered important information of the

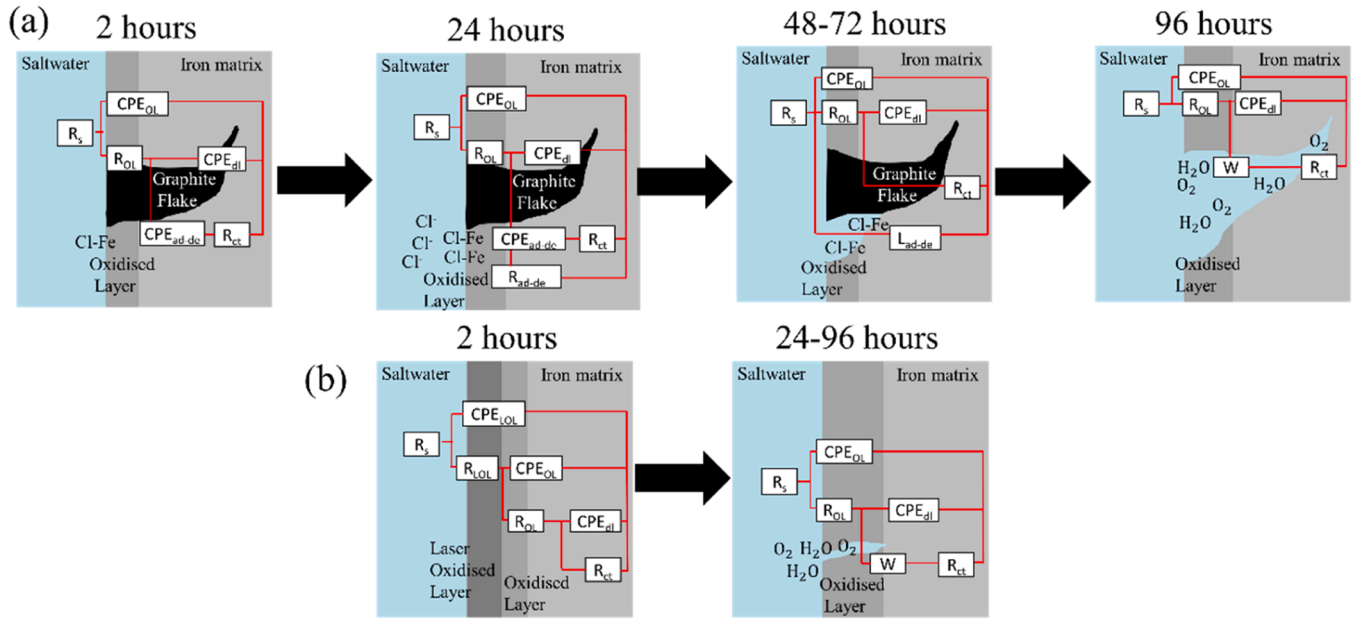

Fig. 14. Schematic drawing of the corrosion mechanisms evolution of the as-received (a) and laser hardened (b) samples in 0.6 M NaCl.

microstructural influence on the corrosion mechanisms and mechanical properties of the samples. The following conclusions were drawn from this study:

1. The size and microstructure generated with the laser can be designed with the parameters (laser beam power, diameter and scan speed). The largest laser hardened zone is produced with 1 mm/s scan speed, 2 mm laser beam diameter and 153.3 W.
2. All laser hardened samples with overlapped scanned tracks are harder than the as-received material. The molten material hardness is higher than that for heat affected zone in the same sample. The samples with an overlap of 25 % are the hardest.
3. The laser hardened samples at 25 % overlap are nobler than the as-received samples and its corrosion rate is slightly lower. The anodic and cathodic branch controls are dissimilar for each sample. As-received sample has an active and passive control for anodic and cathodic branch, respectively, while the laser hardened samples presented diffusion and activation control for the same branches.
4. The corrosion mechanism evolves over time with dissimilar behaviour according to the samples. The laser hardened specimen has a more stable corrosion mechanism over time than as-received material. This is due to the graphite flakes present in as-received material. These encourage the adsorption-desorption process.

In conclusion, this study has showed that the laser hardened process with scans at 25 % overlap can improve both the hardness and corrosion resistance of the material. This is advance on the material processing technology that is of high interest for various industries, such as construction, automotive and machining. The enhancement in the corrosion resistance and hardness can significantly extend the service time and industrial application range for the grey cast iron. Additionally, these improvements enable its use under new operating conditions (e.g., maritime and chemical), thereby increasing its appeal to a boarder range of industries. This study has also provided important information to understand the corrosion mechanism of grey cast iron and the effect of the laser hardening on the corrosion. By shedding light on these aspects, it contributes to addressing fundamental questions in corrosion research.

Funding

The authors declare that no funds, grants, or other support were received during the preparation of this manuscript.

CRediT authorship contribution statement

Ahuir-Torres Juan Ignacio: Writing – review & editing, Writing – original draft, Validation, Supervision, Methodology, Investigation, Formal analysis, Conceptualization. **Meredith Alfred:** Investigation, Data curation. **Batako Andre:** Writing – review & editing, Conceptualization. **Kotadia Hiren:** Writing – review & editing. **Opoz Tahsin Tecelli:** Writing – review & editing. **Zhu Gungyu:** Writing – review & editing. **Khidasheli Nugzar:** Writing – review & editing. **Sharp Martin Charle:** Writing – review & editing. **Bakradze Nana:** Writing – review & editing.

Declaration of Competing Interest

The authors declare that they have no known competing financial interests or personal relationships that could have appeared to influence the work reported in this paper.

Data availability

Data will be made available on request.

References

[1] L. Collini, G. Nicoletto, R. Konečná, Microstructure and mechanical properties of pearlitic gray cast iron, Mater. Sci. Eng.: A 488 (2008) 529–539.
[2] P. Tonolini, L. Montesano, A. Pola, G. Bontempi, M. Gelfi, Wear behavior of Nb alloyed gray cast iron for automotive brake disc application, Metals 13 (2023) 365.
[3] B. Wang, Y. Pan, Y. Liu, N. Lyu, G.C. Barber, R. Wang, W. Cui, F. Qiu, M. Hu, Effects of quench-tempering and laser hardening treatment on wear resistance of gray cast iron, J. Mater. Res. Technol. 9 (2020) 8163–8171.
[4] Q. Sai, J. Hao, S. Wang, Z. Wang, Improving the properties of gray cast iron by laser surface modification, Materials 16 (2023) 5533.
[5] N. Catalán, E. Ramos-Moore, A. Boccardo, D. Celentano, Surface laser treatment of cast irons: a review, Metals 12 (2022) 562.
[6] M.F. Aswad, A.J. Mohammed, S.R. Faraj, Induction Surface Hardening: a review. Journal of Physics: Conference Series, IOP Publishing, 2021 012087.
[7] J. Liu, C. Ye, Y. Dong, Recent development of thermally assisted surface hardening techniques: a review, Adv. Ind. Manuf. Eng. 2 (2021) 100006.
[8] C. Jegadheesan, P. Somasundaram, P. Kumar, A.P. Singh, N. Jeyaprakash, State of art: Review on laser surface hardening of alloy metals, Mater. Today.: Proc. (2023).
[9] R. Ganeev, Low-power laser hardening of steels, J. Mater. Process. Technol. 121 (2002) 414–419.
[10] J.-H. Hwang, D.-Y. Kim, J.-G. Youn, Y.-S. Lee, Laser surface hardening of gray cast iron used for piston ring, J. Mater. Eng. Perform. 11 (2002) 294–300.
[11] S.S. Joshi, D. Choudhuri, S.A. Mantri, R. Banerjee, N.B. Dahotre, S. Banerjee, Rationalizing surface hardening of laser glazed grey cast iron via an integrated experimental and computational approach, Mater. Des. 156 (2018) 570–585.
[12] S.R. Al-Sayed, A.M. Elshazli, A.H.A. Hussein, Laser surface hardening of Ni-hard white cast iron, Metals 10 (2020) 795.
[13] E. Hurtado-Delgado, L. Huerta-Larumbe, A. Miranda-Pérez, Á. Aguirre-Sánchez, Microcracks reduction in laser hardened layers of ductile iron, Coatings 11 (2021) 368.
[14] A. Liu, B. Previtali, Laser surface treatment of grey cast iron by high power diode laser, Phys. Procedia 5 (2010) 439–448.
[15] F.M. Ghaini, M. Ameri, M. Torkamany, Surface transformation hardening of ductile cast iron by a 600w fiber laser, Optik 203 (2020) 163758.
[16] H.R.Abd Ali, E.A. Khalid, A.S. Alwan, A.A. Jaddoa, Effect of fibre laser surface treatment on wear resistance of gray cast iron astm A48, J. Mech. Eng. Res. Dev. 44 (2021) 141–149.
[17] M.S.Fd Lima, F.A. Goia, R. Riva, A.Md Espírito Santo, Laser surface remelting and hardening of an automotive shaft sing a high-power fiber laser, Mater. Res. 10 (2007) 461–467.
[18] I. Pinahin, V. Chernigovskij, A. Bracihin, M. Yagmurov, Improvement of wear resistance of VK6, VK8, T5K10, and T15K6 hard alloys by volume pulsed laser hardening, J. Frict. Wear 36 (2015) 330–333.
[19] J. Wang, J. Xia, Z. Liu, L. Xu, J. Liu, Y. Xiao, J. Gao, H. Ru, J. Jiao, A comprehensive review of metal laser hardening: mechanism, process, and applications, Int. J. Adv. Manuf. Technol. (2024) 1–29.
[20] Ł. Łach, Recent advances in laser surface hardening: Techniques, modeling approaches, and industrial applications, Crystals 14 (2024) 726.
[21] J. Volpp, H.S. Dewi, A. Fischer, T. Niendorf, Influence of complex geometries on the properties of laser-hardened surfaces, Int. J. Adv. Manuf. Technol. 107 (2020) 4255–4260.
[22] S. T. Faris, H.S. Mahdi, K. N. Abed, Studying and Improving the Hardness Properties of Gray Cast Iron, Diyala J. Eng. Sci. (2022) 114–121.
[23] S.K. Fayyadh, E.A. Khalid, A.S. Alwan, Enhancement of Mechanical Properties and Corrosion Resistance of Cast Iron Alloy Using CO2 Laser Surface Treatment, (2022).
[24] N. Maharjan, V.K. Murugan, W. Zhou, M. Seita, Corrosion behavior of laser hardened 50CrMo4 (AISI 4150) steel: a depth-wise analysis, Appl. Surf. Sci. 494 (2019) 941–951.
[25] M. Moradi, D. Ghorbani, M.K. Moghadam, M. Kazazi, F. Rouzbahani, S. Karazi, Nd: YAG laser hardening of AISI 410 stainless steel: microstructural evaluation, mechanical properties, and corrosion behavior, J. Alloy. Compd. 795 (2019) 213–222.
[26] Y. Huang, C. Zhang, Y. Luo, C. Su, N. Guo, N. Li, S. Guo, Enhancing the corrosion properties and microhardness of titanium alloy by laser surface remelting, J. Alloy. Compd. 1008 (2024) 176789.
[27] D. Patel, P. Nanavati, C. Chug, Effect of Ca and Ba Containing Ferrosilicon Inoculants on Microstructure and Tensile Properties of IS-210, and IS-1862 Cast Irons.
[28] J.I. Ahuir-Torres, A.D. Batako, N. Khidasheli, N. Bakradze, G. Zhu, Improving commercial motor bike rim disc hardness using a continuous-wave infrared fibre laser, J. Manuf. Mater. Process. 8 (2024) 18.
[29] L. Convert, E. Bourillot, M. François, N. Pocholle, F. Baras, O. Politano, S. Costil, Laser textured titanium surface characterization, Appl. Surf. Sci. 586 (2022) 152807.
[30] J. Ahuir-Torres, M. Sharp, N. Bakradze, A. Batako, Microstructural design of the cast iron via laser hardening with defocused beam of the continuous wave CO2 laser. Journal of Physics: Conference Series, IOP Publishing, 2022 012048.
[31] M. Moradi, E. Golchin, Investigation on the effects of process parameters on laser percussion drilling using finite element methodology; statistical modelling and optimization, Lat. Am. J. Solids Struct. 14 (2017) 464–484.
[32] A.G. Demir, P. Colombo, B. Previtali, From pulsed to continuous wave emission in SLM with contemporary fiber laser sources: effect of temporal and spatial pulse overlap in part quality, Int. J. Adv. Manuf. Technol. 91 (2017) 2701–2714.

[33] A. International, Standard Practice for Microetching Metals and Alloys Produced by ASTM, ASTM International, 2011.
[34] W. Suder, S. Williams, Investigation of the effects of basic laser material interaction parameters in laser welding, J. Laser Appl. 24 (2012).
[35] N. Catalán, E. Ramos-Moore, A. Boccardo, D. Celentano, N. Alam, M. Walczak, D. Gunasegaram, Surface Laser Treatment on Ferritic Ductile Iron: Effect of Linear Energy on Microstructure, Chem. Compos., Hardness, Metall. Mater. Trans. B 52 (2021) 755–763.
[36] Y. Lua, H. Meyerb, T. Radela, Influence of multi-pass laser hardening on residual stress and distortion.
[37] G. Balachandran, A. Vadiraj, B. Sharath, B. Krishnamurthy, Studies on induction hardening of gray iron and ductile iron, Trans. Indian Inst. Met. 63 (2010) 707–713.
[38] S.-H. Choo, S. Lee, S.-J. Kwon, Surface hardening of a gray cast iron used for a diesel engine cylinder block using high-energy electron beam irradiation, Metall. Mater. Trans. A 30 (1999) 1211–1221.
[39] F. Ayob, P. Hussain, M. Awang, M. Zoolfakar, A. Abdullah, B. Baharudin, A. A. Rahim, Effect of post heat treatment on the microstructure and microhardness of diffusion coupled gray cast iron and low carbon steel. IOP Conference Series: Materials Science and Engineering, IOP Publishing, 2018 012001.
[40] C. Li, Y. Wang, Z. Zhang, B. Han, T. Han, Influence of overlapping ratio on hardness and residual stress distributions in multi-track laser surface melting roller steel, Opt. Lasers Eng. 48 (2010) 1224–1230.
[41] G. Berthomé, B. Malki, B. Baroux, Pitting transients analysis of stainless steels at the open circuit potential, Corros. Sci. 48 (2006) 2432–2441.
[42] Z. Zhang, X. Yuan, Z. Zhao, X. Li, B. Liu, P. Bai, Electrochemical noise comparative study of pitting corrosion of 316L stainless steel fabricated by selective laser melting and wrought, J. Electroanal. Chem. 894 (2021) 115351.
[43] E.-S.M. Sherif, H.S. Abdo, A.A. Almajid, Corrosion behavior of cast iron in freely aerated stagnant Arabian Gulf seawater, Materials 8 (2015) 2127–2138.
[44] E. García-Ochoa, J. González-Sánchez, F. Corvo, Z. Usagawa, L. Dzib-Pérez, A. Castañeda, Application of electrochemical noise to evaluate outdoor atmospheric corrosion of copper after relatively short exposure periods, J. Appl. Electrochem. 38 (2008) 1363–1368.
[45] J. De Damborenea, J. Gonzalez, A. Vazquez, Corrosion behaviour of grey cast iron after laser surface treatment, J. Mater. Sci. Lett. 7 (1988) 1046–1047.
[46] A. Basak, N. Diomidis, J.-P. Celis, C. Masquelier, D. Warichet, Chemical reactivity of thermo-hardenable steel weld joints investigated by electrochemical impedance spectroscopy, Electrochim. Acta 53 (2008) 7575–7582.
[47] J. Ahuir-Torres, S. Simandjuntak, N. Bausch, A. Farrar, S. Webb, A. Nash, B. Thomas, J. Muna, C. Jonsson, D. Matthew, Corrosion threshold data of metallic materials in various operating environment of offshore wind turbine parts (tower, foundation, and nacelle/gearbox), Data Brief. 25 (2019) 104207.
[48] J.I. Ahuir-Torres, G.J. Gibbons, G. West, A. Das, H.R. Kotadia, Understanding the corrosion behaviour of Al-Mg alloy fabricated using a Laser Powder Bed Fusion (L-PBF) Additive Manufacturing (AM) process, J. Alloy. Compd. 969 (2023) 172300.
[49] S. Esmailzadeh, M. Aliofkhazraei, H. Sarlak, Interpretation of cyclic potentiodynamic polarization test results for study of corrosion behavior of metals: a review, Prot. Met. Phys. Chem. Surf. 54 (2018) 976–989.
[50] M.A. Rodríguez, R.M. Carranza, R.B. Rebak, Passivation and depassivation of alloy 22 in acidic chloride solutions, J. Electrochem. Soc. 157 (2009) C1.
[51] D.A. Fischer, I.T. Vargas, G.E. Pizarro, F. Armijo, M. Walczak, The effect of scan rate on the precision of determining corrosion current by Tafel extrapolation: A numerical study on the example of pure Cu in chloride containing medium, Electrochim. Acta 313 (2019) 457–467.
[52] A.H. Seikh, A. Sarkar, J.K. Singh, S.M.K. Mohammed, N. Alharthi, M. Ghosh, Corrosion characteristics of copper-added austempered gray cast iron (AGCI), Materials 12 (2019) 503.
[53] S.A. Ajeel, S.M. Hasoni, Ductile and gray cast irons deterioration with time in various NaCl salt concentrations, Eng. Technol. J. 26 (2008) 154–168.
[54] S. Esmailzadeh, M. Aliofkhazraei, H. Sarlak, Interpretation of cyclic potentiodynamic polarization test results for study of corrosion behavior of metals: a review, Prot. Met. Phys. Chem. Surf. 54 (2018) 976–989.
[55] S. Wang, J. Zhang, O. Gharbi, V. Vivier, M. Gao, M.E. Orazem, Electrochemical impedance spectroscopy, Nat. Rev. Methods Prim. 1 (2021) 41.
[56] H.S. Magar, R.Y. Hassan, A. Mulchandani, Electrochemical impedance spectroscopy (EIS): Principles, construction, and biosensing applications, Sensors 21 (2021) 6578.
[57] V. Vivier, M.E. Orazem, Impedance analysis of electrochemical systems, Chem. Rev. 122 (2022) 11131–11168.
[58] A. Thapa, H. Gao, Low-frequency inductive loop and its origin in the impedance spectrum of a graphite anode, J. Electrochem. Soc. 169 (2022) 110535.
[59] B. Yilbas, I. Toor, C. Karatas, J. Malik, I. Ovali, Laser treatment of dual matrix structured cast iron surface: corrosion resistance of surface, Opt. Lasers Eng. 64 (2015) 17–22.
[60] H.H. Hernández, A.R. Reynoso, J.T. González, C.G. Morán, J.M. Hernández, A. M. Ruiz, J.M. Hernández, R.O. Cruz, Electrochemical impedance spectroscopy (EIS): A review study of basic aspects of the corrosion mechanism applied to steels, Electrochem. Impedance Spectrosc. (2020) 137–144.
[61] E. McCafferty, Introduction to Corrosion Science, Springer Science & Business Media, 2010.
[62] Y. Li, J. Cai, L. Guan, G. Wang, pH-dependent electrochemical behaviour of Al3Mg2 in NaCl solution, Appl. Surf. Sci. 467 (2019) 619–633.
[63] A. Jimenez-Morales, J. Galvan, R. Rodriguez, J. De Damborenea, Electrochemical study of the corrosion behaviour of copper surfaces modified by nitrogen ion implantation, J. Appl. Electrochem. 27 (1997) 550–557.
[64] R. Logan, M. Mulheron, D. Jesson, P. Smith, T. Evans, N. Clay-Michael, J. Whiter, Graphitic corrosion of a cast iron trunk main: implications for asset management, WIT Trans. Built Environ. (2014) 139.
[65] H. Guo, H. Chen, H. Zhang, X. Liu, Y. Chen, Y. Tian, J. Yin, Study on growth of corrosion scale on various iron based materials (grey cast iron/carbon steel/ductile iron) in water distribution systems, Int. J. Electrochem. Sci. 15 (2020) 8479–8497.
[66] I. Frateur, C. Deslouis, M. Orazem, B. Tribollet, Modeling of the cast iron/drinking water system by electrochemical impedance spectroscopy, Electrochim. Acta 44 (1999) 4345–4356.